Astronomy & Astrophysics manuscript no. torsionfin
January 27, 2022

Angular momentum transport by magnetoconvection and the magnetic modulation of the solar differential rotation

G. Rüdiger[1,2] and M. Küker[1]

[1] Leibniz-Institut für Astrophysik Potsdam (AIP), An der Sternwarte 16, D-14482 Potsdam, Germany,
[2] University of Potsdam, Institute of Physics and Astronomy, D-14476 Potsdam, Germany

Received; accepted

ABSTRACT

In order to explain the variance of the solar rotation law during the activity minima and maxima, the angular momentum transport by rotating magnetoconvection is simulated in a convective box penetrated by an inclined azimuthal magnetic field. Turbulence-induced kinetic and magnetic stresses and the Lorentz force of the large-scale magnetic background field are the basic transporters of angular momentum. Without rotation, the sign of the magnetic stresses naturally depends on the signs of the field components as positive (negative) $B_\theta B_\phi$ transport the angular momentum poleward (equatorward). For fast enough rotation, however, the turbulence-originated Reynolds stresses start to dominate the transport of the angular momentum flux. The simulations show that positive ratios of the two meridional magnetic field components to the azimuthal field reduce the inward radial as well as the equatorward latitudinal transport,which result from hydrodynamic calculations. Only for $B_\theta B_\phi > 0$ (generated by solar-type rotation laws with an accelerated equator) does the magnetic-influenced rotation at the solar surface prove to be flatter than the nonmagnetic profile together with the observed slight spin-down of the equator. The latter phenomenon does not appear for antisolar rotation with polar vortex as well as for rotation laws with prevailing radial shear.

Key words. Magnetic fields – angular momentum transport – convection

1. Introduction

The solar surface rotation law exhibits a correlation with solar activity parameters such as sunspot numbers, large-scale magnetic fields, or small bright coronal structures (SBCS). Equatorial rotation is faster during the activity minimum and slower in the activity maximum. The magnetic field seems to decelerate the solar equator (Gilman & Howard 1984; Jurdana-Šepić et al. 2011). This deceleration might be interpreted as a magnetic-originated reduction of the radial shear provided the radial profile $\Omega = \Omega(r)$ increases outwards ('superrotation') while the lower value $\Omega_{\rm in}$ is fixed by the tachocline at the bottom of the convection zone.

Simultaneously, the form of the latitudinal rotation law $\Omega = \Omega(\theta)$ at the surface also varies with the phase of the activity cycle. The latitudinal shear is reduced by the magnetic field, that is to say it is larger during the minimum activity and it is smaller during the maximum activity (Ruždjak et al. 2017).

The numbers, however, are small. Expressed with the traditional definition

$$\Omega = A + B\cos^2\theta \tag{1}$$

(with A being the equatorial rotation rate and with θ being the colatitude), the variation of A is about 1% while B varies by about 20% between activity minimum and activity maximum (Xie et al. 2018). The latter value implies that the normalised equator-pole difference of the surface rotation, $a = \delta\Omega/\Omega > 0$, varies in time by about 3%. We write

$$\Delta A = A_{\rm max} - A_{\rm min}, \qquad \Delta a = a_{\rm max} - a_{\rm min}, \tag{2}$$

where the suffixes max and min concern the rotation laws with and without a magnetic field. The observed differences ΔA and Δa are both negative, hence

$$\Delta A \cdot \Delta a > 0, \qquad \frac{\Delta a}{\Delta A} \simeq 3. \tag{3}$$

The magnetic field both reduces the equatorial angular velocity and the latitudinal shear, but the magnetic-induced reduction of the equatorial velocity is weaker than that of the pole-equator difference. We shall explain these observational findings by calculating the angular momentum transport in rotating convective boxes under the influence of a strong azimuthal magnetic field combined with weak meridional components. The Lorentz force of this field as well as the anisotropic Reynolds stresses are the main transporters of angular momentum (Malkus & Proctor 1975; Kitchatinov et al. 1994). We shall see that only one of the possible magnetic configurations provides rotation laws fulfilling the conditions (3). It is just this configuration ($B_\theta B_\phi > 0$) which is a natural outcome of all $\alpha\Omega$ dynamos which operate with solar-type rotation laws, that is to say with an accelerated equator. Toroidal fields induced by negative radial shear produce the opposite sign, that is $B_r B_\phi < 0$.

With their anelastic spherical harmonic (ASH) code, Brun et al. (2004) demonstrate that the simulated rotation laws at the surface of the convection zone indeed strongly vary for magnetic models and purely hydrodynamic calculation. Both the pole-equator difference of the rotation rate and also its equatorial value are reduced by the dynamo-excited magnetic fields. Also the simulations by Karak et al. (2015), Augustson et al. (2015), Käpylä et al. (2016), and Warnecke et al. (2018) provide reduced equatorial rotation rates during the magnetic maximum. In some of these calculations, the Maxwell stress of the induced large-scale magnetic fields only plays a minor role in the transportation of angular momentum. Because of the complexity of the numerical magnetohydrodynamic simulations (see also Browning et al.

(2006)), it remains unclear, however, by which mechanism the magnetic field suppresses the non-uniformity of the rotation laws which, in hydrodynamics, is maintained by Reynolds stresses due to the anisotropy of the underlying turbulence.

Brun et al. (2004) prescribe dissipation of the angular momentum by unresolved modes by fixing a magnetically uninfluenced eddy viscosity of 10^{12} cm^2/s, which also determines the resulting meridional flow. Consequently, the isolines of the resulting rotation law are more or less cylindrical because of the Taylor-Proudman theorem. Kippenhahn (1963) demonstrated the basic physics: If a turbulence transports angular momentum, for instance, outwards, then the resulting super-rotating rotation law with spherical Ω isolines induces a clockwise meridional circulation (in the northern hemisphere) transporting angular momentum to the equator. The Ω isolines become cylindrical as is also the case in many simulations (see recent papers by Featherstone & Miesch 2015; Warnecke 2018; Warnecke et al. 2018). In mean-field models, anisotropic heat transport due to rotating convection which produces 'warm' poles overcomes the Taylor-Proudman theorem (Kitchatinov & Rüdiger 1995), while in numerical simulations the poles must additionally be warmed up (Browning et al. 2006; Miesch et al. 2006).

By a combination of local box simulations (Section 5) and global mean-field equations (Section 6), we shall demonstrate with the present paper that the observed finding (3) can be explained by the magnetic influence of the dynamo-induced large-scale fields onto the rotation-induced non-diffusive parts of the Reynolds stresses (the 'Lambda-effect'). The Maxwell stress of the large-scale fields (the 'Malkus-Proctor effect'), however, appears to play only a minor role. This explanation only succeeds for positive product $B_\theta B_\phi$ of the meridional magnetic field component B_θ and the toroidal magnetic field component B_ϕ. Just this condition is fulfilled if positive latitudinal shear on the northern hemisphere and negative latitudinal shear on the southern hemisphere is responsible for the induction of the toroidal fields, which indeed complies with the observations.

2. Angular momentum transport

Both turbulence-originated Reynolds stress and Maxwell stress must be formulated for a turbulent fluid under the presence of a uniform background field vector $\boldsymbol{B}$. The fluctuating flow and field components are denoted by $\boldsymbol{u}$ and by $\boldsymbol{b}$, respectively. The standard Maxwell tensor

$$M_{ij} = \frac{1}{\mu_0} B_i B_j - \frac{1}{2\mu_0} \boldsymbol{B}^2 \delta_{ij} \tag{4}$$

of the large-scale field turns into the generalised stress tensor

$$M_{ij}^{\rm tot} = M_{ij} + M_{ij}^{\rm T}, \tag{5}$$

with the turbulence-induced Maxwell tensor

$$M_{ij}^{\rm T} = \frac{1}{\mu_0} \langle b_i(\boldsymbol{x},t) b_j(\boldsymbol{x},t) \rangle - \frac{1}{2\mu_0} \langle \boldsymbol{b}^2(\boldsymbol{x},t) \rangle \delta_{ij}. \tag{6}$$

The negative coefficients of the Kronecker tensors in Eq. (5) form the total pressure which we can completely ignore in what follows. The difference between the Reynolds tensor and Maxwell tensor is

$$T_{ij}^{\rm T} = Q_{ij} - \frac{1}{\rho} M_{ij}^{\rm T} \tag{7}$$

with the one-point correlation tensor being $Q_{ij} = \langle u_i(\boldsymbol{x},t) u_j(\boldsymbol{x},t) \rangle$ of the flow. The expression

$$T_{ij} = T_{ij}^{\rm T} - \frac{1}{\rho} M_{ij} \tag{8}$$

gives the total contribution of turbulence and magnetic background fields to the angular momentum transport. The off-diagonal components

$$T_{r\phi} = Q_{r\phi} - \frac{1}{\mu_0 \rho} \langle b_r(\boldsymbol{x},t) b_\phi(\boldsymbol{x},t) \rangle - \frac{1}{\mu_0 \rho} B_r B_\phi \tag{9}$$

and

$$T_{\theta\phi} = Q_{\theta\phi} - \frac{1}{\mu_0 \rho} \langle b_\theta(\boldsymbol{x},t) b_\phi(\boldsymbol{x},t) \rangle - \frac{1}{\mu_0 \rho} B_\theta B_\phi \tag{10}$$

represent the fluxes of specific angular momentum in the radial and latitudinal direction by the magnetoconvection under the influence of a magnetic background field. The quantities do not contain pressure terms. Expressions 9 and 10 for purely azimuthal fields have already been calculated for stellar convection under the presence of a purely azimuthal magnetic field where surprisingly a magnetic quenching of the turbulent fluxes of angular momentum did not appear (Käpylä et al. 2004).

It is known that the symmetry of the cross-correlations $T_{r\phi}$ and $T_{\theta\phi}$ differs from that of all other components of the tensor T_{ij}. While $T_{r\phi}$ and $T_{\theta\phi}$ are antisymmetric with respect to the transformation $\Omega \to -\Omega$, all other correlations are not. The turbulent angular momentum transport is thus odd in Ω, while the other terms – the cross-correlation $T_{r\theta}$ included – are even in Ω. It is easy to show that $T_{r\phi}$ is symmetric with respect to the equator if the averaged flow and the magnetic fields are also symmetric. Then the component $T_{\theta\phi}$ is antisymmetric with respect to the equator. These rules can only be violated if, for example, the magnetic field strengths in the two hemispheres are different.

One can easily show that isotropic turbulence even under the influence of rotation does not lead to finite values of $T_{r\phi}$ and $T_{\theta\phi}$. Only with a preferred direction $\boldsymbol{g}$ can a tensor $(\epsilon_{ikl} g_j + \epsilon_{jkl} g_i) g_k \Omega_l$ linear in Ω exist, possessing cross-correlations with the index ϕ as one of the indices (if $\boldsymbol{g}$ is radially directed). Rigidly rotating anisotropic turbulence, therefore, is thus able to transport angular momentum ('Λ effect').

As in Rüdiger et al. (1986), we write

$$\mu_0 M_{ij}^{\rm T} = \kappa' \boldsymbol{B}^2 \delta_{ij} - \kappa B_i B_j \tag{11}$$

($\kappa > 0$ for $\Omega = 0$) so that

$$\mu_0 M_{ij}^{\rm tot} = \kappa' \boldsymbol{B}^2 \delta_{ij} + (1-\kappa) B_i B_j \tag{12}$$

for the sum of small-scale and large-scale Maxwell stresses. For the nonrotating fluid, the one-point-correlation tensor may be written as

$$Q_{ij} = Q_{ij}^{(0)} + D' \frac{\boldsymbol{B}^2}{\mu_0 \rho} \delta_{ij} + D \frac{B_i B_j}{\mu_0 \rho} \tag{13}$$

with $Q_{ij}^{(0)}$ for $\boldsymbol{B} = 0$. A vertical magnetic field supports the vertical turbulence intensity (Chandrasekhar 1961), which is described by $D > 0$. It follows that

$$T_{xz} = T_{xz}^* + D^* \frac{B_x B_z}{\mu_0 \rho}, \qquad T_{yz} = T_{yz}^* + D^* \frac{B_y B_z}{\mu_0 \rho} \tag{14}$$

with $D^* = D + \kappa - 1$. In accordance with the geometry of the box simulations presented below, here, we introduced the coordinates (x, y, z) as local Cartesian proxies of the global spherical coordinates (r, θ, ϕ).

We note that the coefficients D and κ of the Reynolds stress and Maxwell stress work in the same direction. The sum $D + \kappa$ describes the turbulence-induced magnetic angular momentum transport which is accompanied by that of the large-scale Lorentz force, that is to say minus 1 in the coefficient of B_xB_z or B_yB_z, respectively. Only the latter terms are odd in the field components B_x and B_y, but not T^* which is even in all single field components by definition. If, therefore, two simulations exist with one and the same B_x, but with opposite B_z, then from Eq. (14) it follows that $T^*_{xz} = (T^+_{xz} + T^-_{xz})/2$ and $D^* = \mu_0\rho(T^+_{xz} - T^-_{xz})/2B_x|B_z|$. To introduce physical units for the intensity quantities, a tilde denotes normalisation with the turbulence intensity $u^2_{\rm rms}$ calculated without rotation and without a field. The sum $D + \kappa$ describes whether the rotating turbulence supports the angular momentum transport by the Lorentz force or not; its sign is not fixed by definition.

The magnetic background field may consist of a dominating azimuthal field B_z together with weak meridional components B_x and B_y forming the inclination ('pitch') angles,

$$p_x = \frac{B_x}{B_z}, \qquad p_y = \frac{B_y}{B_z}, \tag{15}$$

(always taken in the northern hemisphere) with $|p_x| \ll 1$ and $|p_y| \ll 1$. We note that for the Sun, $p_y > 0$ at the northern hemisphere since, as generally believed, the toroidal large-scale magnetic field B_z is generated from the latitudinal field B_y by a latitude-dependent rotation law with an accelerated equator. Antisolar rotation leads to $p_y < 0$. The negative radial shear in the solar subsurface shear layer would produce negative values of p_x. Because of the magnetic feedback, the winding-up process is almost independent of the seed field B_y. One finds $B_z \simeq \delta\Omega L\sqrt{\mu_0\rho}$ with $\delta\Omega$ as the differential rotation and L as the characteristic length scale so that for the Sun $B_z \lesssim 10^4$ G. Together with the observed poloidal field strength, $p_y \gtrsim 10^{-4}$. In the spirit of Lenz's rule, we expect that fields with positive p_y lead to rotation laws with less latitudinal shear than the nonmagnetic system would produce. We shall indeed show that both the inclinations p_x and p_y are able to reduce the nonmagnetic surface shear of the differential rotation, but only a positive p_y simultaneously reduces the equatorial rotation rate as observed in the cycle maxima.

3. No rotation

To study the effect of the magnetic field on the angular momentum transport quantitatively, we ran a series of direct numerical simulations to study convection in a rotating rectangular box. The Nirvana code uses a Godunov scheme as described in Ziegler (2004) to solve the equations of energy conservation and mass conservation, the equation of motion, and the induction equation. The model assumes a fully ionised ideal gas with constant specific heat capacity. The stratification of the gas is piecewise polytropic,

$$\frac{\partial \ln P}{\partial \ln T} = m + 1. \tag{16}$$

A convectively unstable layer with $m = 1$ was placed between two stably stratified layers with $m = 9$. The heat flux is constant throughout the simulation box. The box size is $L_x \times L_y \times L_z = 2 \times 6 \times 6$ in dimensionless units. The unstable layer starts at $x = 0.8$ and ends at $x = 1.8$. The boundary conditions in the horizontal y and z directions are periodic. On the lower boundary ($x = 0$), we imposed a fixed temperature, no penetration, stress-free horizontal flow, and pseudo-vacuum boundary conditions on the magnetic field. On the upper boundary at $x = 2$, the boundary conditions imply a fixed temperature gradient, while the boundary conditions on the gas flow and the magnetic field are the same as on the lower boundary. The mesh size is $N_x \times N_y \times N_z = 128 \times 384 \times 384$. The simulations start with hydrostatic equilibrium and a small random perturbation and run for about 200 turnover times. The Rayleigh number in the unstable layer is $\mathrm{Ra} = 10^7$. The ratio of the densities at the bottom and top of the simulation box is (only) 5.8. In code units, the isothermal sound speed is $c_{\rm ac} = 100$ at the top of the unstably stratified layer, and the viscosity is 6.32×10^{-3} while those of the magnetic diffusivity and the heat diffusion coefficient are 6.32×10^{-2}. The magnetic field was imposed as an initial condition and periodically reset. It is constant in the vertical (x) direction while the boundary conditions require the horizontal field components to be zero on the upper and lower boundaries. These components therefore vary with depth, that is

$$B_y, B_z \propto \sin\left(\frac{\pi x}{2}\right). \tag{17}$$

The below mentioned field amplitudes B_y and B_z always refer to the maxima in the centre of the box. If the above introduced Lorentz force factor D is defined for uniform fields, then the D for the simulated nonuniform fields thus slightly depends on the radial profile used in Eq. (17). The background field was introduced as an initial condition and reset after each snapshot. This kept the vertical (x) and toroidal (z) components close to the initial configuration. For the y-component, however, the time between snapshots proved sufficient to develop a significant departure, which limited our ability to apply weak fields in that direction, as discussed below.

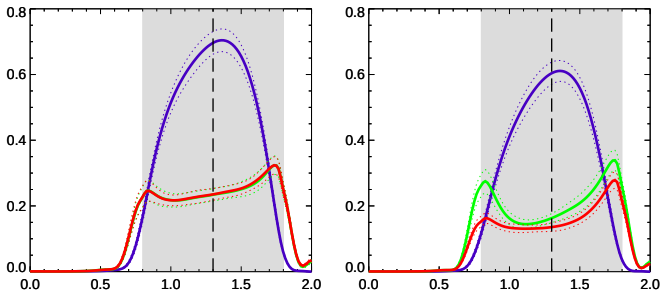

Fig. 1. Turbulent intensities by nonrotating convection without (left panel) and with a magnetic field (right panel, $\boldsymbol{B} = (0, 1, 10)$); $\tilde{Q}_{xx}$ (blue line), $\tilde{Q}_{yy}$ (green line), and $\tilde{Q}_{zz}$ (red line) as a function of the vertical coordinate x. In the left panel, the red line hides the green line. The convectively unstable part of the box is grey-shaded; $\Omega = 0$, $\mathrm{Pr} = 0.1$, and $\mathrm{Pm} = 0.1$.

Without a magnetic field, the turbulence in the horizontal plane is isotropic hence the $Q_{yy} = Q_{zz}$. A magnetic field along a coordinate axis forms an anisotropy in the horizontal plane and $Q_{yy} \neq Q_{zz}$. For the magnetic fields $\boldsymbol{B} = (0, 1, 10)$, the normalised autocorrelations $\tilde{Q}_{xx}$, $\tilde{Q}_{yy}$, and $\tilde{Q}_{zz}$ are plotted in Fig. 1. One finds all the intensities to be reduced by the magnetic field where the degree of quenching grows for the stronger field component (red curve). By the magnetic influence, the horizontal intensity excess $Q_{yy} - Q_{zz}$ becomes positive. The normalised numerical value is $\tilde{Q}_{yy} - \tilde{Q}_{zz} \simeq 0.045$.

Next the cross-correlations Q_{xz} and Q_{yz} for nonrotating magnetoconvection are discussed. As known within the quasilinear

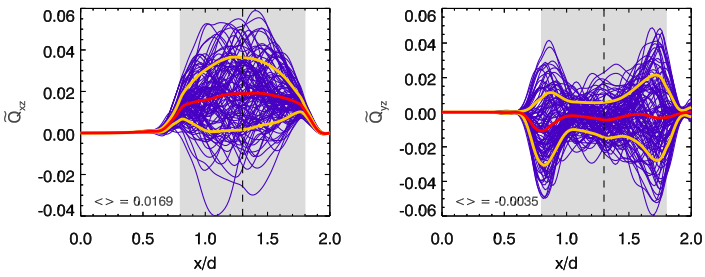

Fig. 2. Left: Vertical cross-correlation $\tilde{Q}_{xz}$ for $\boldsymbol{B} = (1, 0, 10)$ (left panel) and the horizontal cross-correlations $\tilde{Q}_{yz}$ for $\boldsymbol{B} = (0, 1, 10)$ (right panel). We note that $\tilde{Q}_{yz}$ is much smaller than $\tilde{Q}_{xz}$ (see Eq. (28)). Each blue line represents the horizontal average over one snapshot. The red lines represent averages over the snapshots, and the yellow lines indicate the standard deviation. The convectively unstable part of the box is grey-shaded. The numbers in ⟨⟩-brackets are the averages taken over the whole unstably stratified layer and over time; $\Omega = 0$, Pr = 0.1, and Pm = 0.1.

approximation, the correlation tensor of a homogeneous turbulence influenced by a weak large-scale magnetic field $\boldsymbol{B}$ is

$$Q_{ij} - Q_{ij}^{(0)} = 2 \int\int \frac{\omega^2 - \nu\eta k^4}{(\omega^2 + \nu^2 k^4)(\omega^2 + \eta^2 k^4)} \frac{(\boldsymbol{kB})^2}{\mu_0 \rho} \hat{Q}_{ij}^{(0)} \, \mathrm{d}\boldsymbol{k} \, \mathrm{d}\omega \tag{18}$$

with $\hat{Q}_{ij}^{(0)}$ as the spectral tensor of the original nonmagnetic turbulence (Rüdiger 1974). For isotropic and incompressible turbulence, the tensor is simply

$$\hat{Q}_{ij}^{(0)}(\boldsymbol{k}, \omega) = \frac{E(k, \omega)}{16\pi k^4} \left(k^2 \delta_{ij} - k_i k_j\right), \tag{19}$$

where the positive-definite spectrum E provides the kinetic energy

$$\langle \boldsymbol{u}^{(0)2} \rangle = \int_0^\infty \int_0^\infty E(k, \omega) \, \mathrm{d}k \, \mathrm{d}\omega. \tag{20}$$

The insertion of Eq. (19) into Eq. (18) and some algebra lead to

$$Q_{ij} = Q_{ij}^{(0)} - Q_3 (2\boldsymbol{B}^2 \delta_{ij} - B_i B_j), \tag{21}$$

where the coefficient Q_3 evaluates to

$$Q_3 = \frac{1}{60\pi\mu_0\rho} \int\int \frac{(\nu\eta k^4 - \omega^2) E(k, \omega)}{(\omega^2 + \nu^2 k^4)(\omega^2 + \eta^2 k^4)} \, \mathrm{d}\boldsymbol{k} \, \mathrm{d}\omega. \tag{22}$$

One finds $Q_3 > 0$ for all spectra monotonously decreasing with increasing frequency. From Eq. (21) for the magnetic-induced anisotropies in the horizontal plane follows

$$Q_{yy} - Q_{zz} = Q_3 (B_y^2 - B_z^2). \tag{23}$$

The turbulence intensity should be increased in the direction of the magnetic field. For dominating B_z, the difference proves to be negative, but it is positive in our simulations (see Fig. 1). For the cross-correlation, one obtains the simple relations

$$Q_{xz} = Q_3 B_x B_z, \qquad Q_{yz} = Q_3 B_y B_z. \tag{24}$$

For positive field components, both cross-correlations should be positive, but only the first of these relations is confirmed by the numerical simulations shown in Fig. 2.

The reason for the discrepancies is the anisotropy of the original turbulence field. For anisotropic turbulence fields, the above model is too simple. To the spectral tensor as shown in Eq. (19), an anisotropic turbulence may be added which, for example, has no velocity components in the $\boldsymbol{g}$ direction, that is

$$\hat{Q}_{ij}^{(0)}(\boldsymbol{k}, \omega) = \frac{E_\perp(k, \omega)}{16\pi k^4} \times \left((k^2 - (\boldsymbol{gk})^2)(\delta_{ij} - g_i g_j) - (k_i - (\boldsymbol{gk}) g_i)(k_j - (\boldsymbol{gk}) g_j)\right). \tag{25}$$

A turbulence with a dominating intensity in the $\boldsymbol{g}$-direction requires $E_\perp < 0$, while $E_\perp > 0$ originates a horizontal turbulence. Furthermore, $E_\perp < 0$ is a necessary condition to describe anisotropic turbulence with dominating vertical intensities.

The total correlation tensor, for example as can be seen in Eq. (21), is completed by

$$Q_{ij} = ... - Q_2 (\frac{3}{2} \boldsymbol{B}^2 (\delta_{ij} - g_i g_j) - (\boldsymbol{gB})^2 \delta_{ij} + (\boldsymbol{gB})(g_i B_j + g_j B_i) - B_i B_j) \tag{26}$$

with Q_2 similar to (22) but with $E_\perp$ instead of E. Furthermore, Q_2 is not positive-definite. We note that the influence of the magnetic field does not provide vertical motions if the turbulence is strictly horizontal. With this turbulence model, Eq. (23) becomes

$$Q_{yy} - Q_{zz} = -(Q_3 + Q_2) B_z^2. \tag{27}$$

Here again $|B_z|$ is assumed to be much larger than the other components. Obviously, the magnetic field in the z direction can increase the anisotropy of the turbulence in favour of the z-component of the velocity. The effect vanishes, however, for $Q_2 + Q_3 \lesssim 0$, that is for turbulence with a dominant vertical intensity. After Eq. (27), the magnetic-induced anisotropy of the turbulence intensity in the horizontal plane changes its sign with the sign of $Q_2 + Q_3$.

For the cross-correlations, that is Eq. (24), it now follows that

$$Q_{xz} = Q_3 B_x B_z, \qquad Q_{yz} = (Q_2 + Q_3) B_y B_z, \tag{28}$$

where the x-direction is parallel to $\boldsymbol{g}$. The first expression remains uninfluenced by the anisotropy, while the second one no longer has a definite sign. We note that the cross-correlations Q_{xz} and Q_{yz} in anisotropic turbulence differ even for identical field strengths and pitch angles. The vertical cross-correlation Q_{xz} exceeds the horizontal cross correlation Q_{yz} if the vertical turbulence intensity exceeds the horizontal one and vice versa. For turbulence with a dominating intensity in the $\boldsymbol{g}$-direction, it is $Q_3 + Q_2 \lesssim 0$ that leads to $Q_{yz} \lesssim 0$, which is confirmed by the simulation results of Fig. 2 with its rather small numerical values of the horizontal cross-correlation Q_{yz}. The correlation Q_{xz} is only due to the isotropic part of the turbulence field and should never vanish if B_x and B_z do not vanish. It only vanishes in a coordinate system with one of the axes parallel to the total magnetic field vector.

The ratio of the cross-correlation to the excess of the auto-correlations results from Eqs. (27) and (28) simply to

$$\frac{Q_{yz}}{Q_{yy} - Q_{zz}} = -\frac{B_y}{B_z}, \tag{29}$$

which after the numerical results in the right panels of Figs. 1 and 2 is well fulfilled. The numbers may also demonstrate the high accuracy of our numerical code.

As the next step, the total horizontal cross component T_{yz} may be calculated for the magneto-convective fluid with no rotation but with $p_y = \pm 0.1$. The total stress can be written as $T_{yz} = Q_{yz} - m_{yz} - M_{yz}$ with Q as the Reynolds stress, m as the small-scale Maxwell stress, and M as the large-scale Lorentz force $M_{yz} = B_y B_z/\mu_0\rho$.

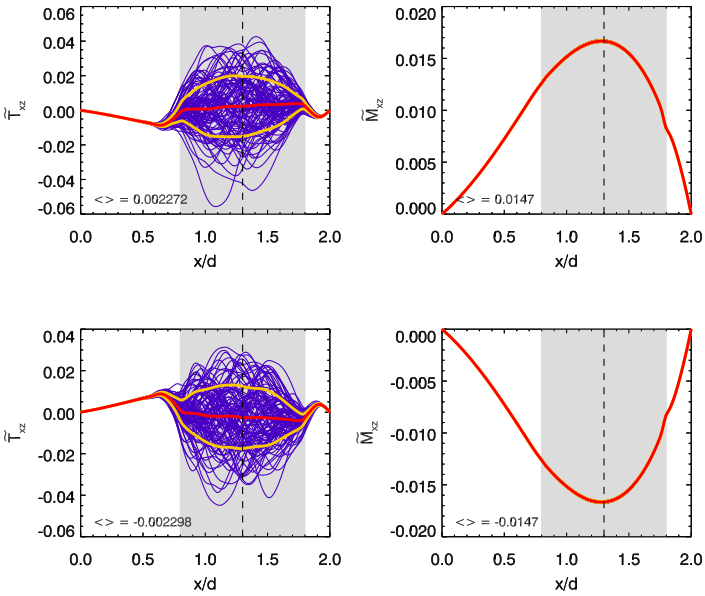

Fig. 3. Snapshots of the $\tilde{T}_{xz}$-correlations (left) and the large-scale Maxwell stress $\tilde{M}_{xz}$ (right) – normalised with $u_{\rm rms}^2 = 28$ – for a nonrotating fluid with magnetic fields $\boldsymbol{B} = (1, 0, 10)$ (top) and $\boldsymbol{B} = (1, 0, -10)$ (bottom). We find the resulting torque $\tilde{T}_{xz}$ to be rather small since Reynolds stress and Maxwell stress nearly cancel each other. The signs of the quantities in the top and the bottom are different; $\Omega = 0$, Pr = 0.1, and Pm = 0.1.

As shown by Figs. 3 and 4, the off-diagonal elements T_{xz} and T_{yz} due to the Reynolds stress and the Maxwell stress exist, but their typical behaviour is different. In contrast to Eq. (24) for isotropic turbulence, the two cross-correlations are not equal by far; T_{xz} is much smaller than T_{yz}. The reason is that $Q_{xz} \simeq M_{xz}$ so that $T_{xz} \simeq 0$, but this is not true for the horizontal correlation (yz). In this case, the Reynolds stress is much smaller than the Maxwell stress hence $T_{yz} \simeq -1.5 M_{yz}$. The horizontal angular momentum transport is mainly due to the large-scale Lorentz force. The contribution of the Reynolds stress to the total stress is only 25% and that of the turbulent Maxwell stress is only 5%. Because of the averaging procedure, the numerical result $\tilde{M}_{yz} \simeq 0.010$ for $B_y = 1$ and $B_z = 10$ is smaller than $\tilde{M}_{yz} \simeq 0.028$ obtained with the amplitudes of B_y and B_z. For simplicity in the following, we shall use the latter expression so that the applied magnetic fields are slightly overestimated compared with the averaged fields.

For toroidal fields B_z with different signs, the two fluxes $\tilde{T}_{yz}$ and $\tilde{T}_{yz}$ also differ by the sign (Fig. 4). Without rotation, we find $\tilde{D}^* \simeq -0.018$, that is $D^* \simeq -0.5$ and $D + \kappa \simeq 0.5$. The density stratification reduces D^* by 50 %, that is from -1 to -0.5. For rotating boxes, the question remains as to how much the magnetic-influenced Reynolds stress influences these results.

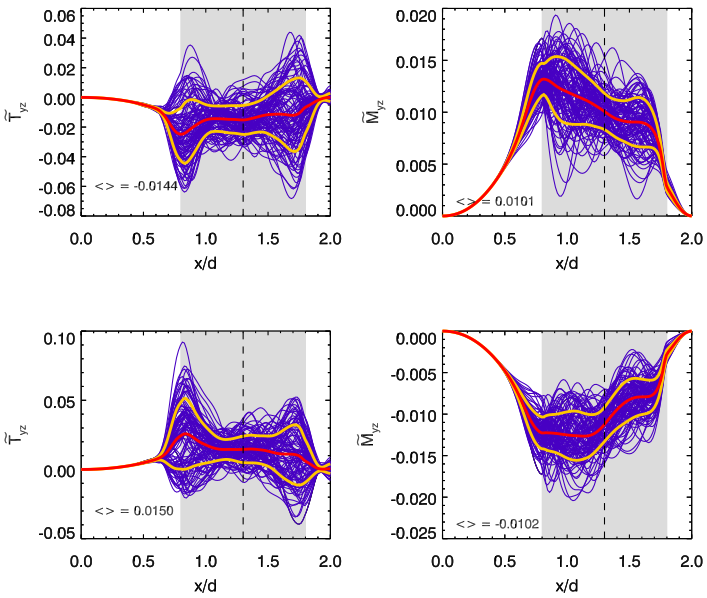

Fig. 4. Similar to Fig. 3, but for the horizontal torque $\tilde{T}_{yz}$ for a nonrotating fluid with a magnetic field $\boldsymbol{B} = (0, 1, 10)$ (top) and $\boldsymbol{B} = (0, 1, -10)$ (bottom). It is $\tilde{T}_{yz} \simeq -\tilde{M}_{yz}$ hence the Reynolds stress is not important. Again the signs of the quantities in the top and the bottom are different; $\Omega = 0$, Pr = 0.1, and Pm = 0.1.

4. Helicity and alpha effect

In rotating boxes also finite values of the α effect should evolve with consequences for the effective large-scale fields. The α effect generates poloidal field components B_y from the toroidal field component B_z, which is always the largest one in the simulations. If, as in our models, only the radial coordinate x serves for the calculations of gradients, then the only relevant component of the induction equation is

$$\frac{\partial B_y}{\partial t} = -\frac{\mathrm{d}}{\mathrm{d}x}(\alpha B_z) + \eta_{\rm T}\frac{\mathrm{d}^2 B_y}{\mathrm{d}x^2}, \qquad (30)$$

where the α represents the $(\phi\phi)$ component, which is the most important one for the $\alpha\Omega$ dynamo mechanism, and the $\eta_{\rm T}$ is the eddy diffusivity. We know that intensity stratifications provide finite values of the α effect as in the well-known relation $\alpha_{\phi\phi} = -\hat{\alpha}\boldsymbol{\Omega}\cdot\nabla u_{\rm rms}$ with positive $\hat{\alpha}$. Because of the radial boundary conditions, the gradient of $u_{\rm rms}$ must be negative (positive) at the top (bottom) of the box. In the northern hemisphere, the resulting α effect is thus always positive (negative) at the top (bottom) of the box. The same argument holds for the helicity $\mathcal{H} = \langle \boldsymbol{u}\cdot\mathrm{curl}\,\boldsymbol{u}\rangle$, but with opposite signs: negative at the top and positive at the bottom. We computed the helicity for fast rotation ($\Omega = 10$) of the magnetised fluid. As expected, the quantity $\mathcal{H}$ is positive (negative) in the lower (upper) part of the numerical box. It vanishes almost exactly at its centre. We also note, as expected, that the helicity at the poles exceeds the helicity of mid-latitudes (Fig. 5).

The rotation rate $\Omega \simeq 10$ represents a Coriolis number of $\Omega^* = 2\tau_{\rm corr}\Omega \simeq 2$ if the correlation time $\tau_{\rm corr} \lesssim 0.1$ is used, which resulted from an autocorrelation analysis of the same numerical convection model (Küker & Rüdiger 2018). We note that $\Omega^* \simeq 2$ is close to the solar value. With the same correlation time, the helicity amplitude of 2.5 in Fig. 5 leads to $\alpha/u_{\rm rms} \simeq 0.05$, which is slightly smaller than what Ossendrijver et al. (2001, 2002) found

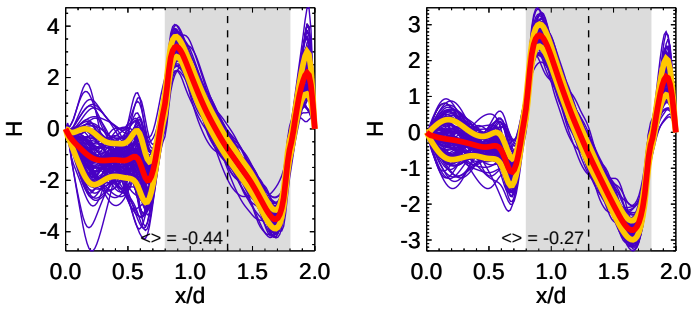

Fig. 5. Snapshots of the small-scale helicity $\mathcal{H}$ at the north pole ($\theta = 0°$, left) and mid-latitudes ($\theta = 45°$, right) for fast rotation. As expected, the helicity vanishes in the middle of the box. The applied magnetic field is $\boldsymbol{B} = (0, 0.1, 10)$, $\Omega = 10$, Pr = 0.1, and Pm = 0.1.

with 10% for rotating magnetoconvection. In their simulations, Käpylä et al. (2009) also found typical values of the order of 10% (see their Fig. 8).

One thus finds unavoidable consequences for the simulations. The α effect automatically generates meridional large-scale fields B_y from the toroidal field B_z in accordance with the stationary induction equation (30), that is $\eta_T \mathrm{d}^2 B_y/\mathrm{d}x^2 = B_z \mathrm{d}\alpha/\mathrm{d}x$. For positive B_z and positive $\mathrm{d}\alpha/\mathrm{d}x$ (α growing with height), the second derivative of B_y is obviously positive. The small-scale α effect, therefore, generates a minimum of B_y between the top and bottom of the box. The Maxwell stress $B_y B_z$, therefore, is reduced compared to its value without rotation; it may even change its sign. The right panel of Fig. 6 demonstrates how the applied value of $B_y = 0.10$ is changed to $B_y = -0.16$ by the action of the α effect so that the simulated cross-correlation T_{yz} is larger than the 'real' one without an α effect.

The right panel of Fig. 6 shows negative B_y in the bulk of the convective box despite the small and positive starting field. Test calculations with $B_z = -10$ provided the opposite sign of the B_y. On the other hand, the radial component B_x proves to be completely uninfluenced (left panel of Fig. 6). The stress components T_{xz} are thus not modified by the small-scale α effect resulting from rotating fluids.

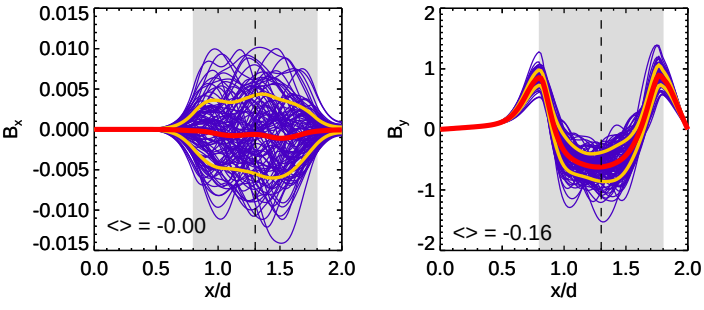

Fig. 6. Snapshots of the large-scale field components B_x (left) and B_y (right) in the box. We note the transformation of $B_y > 0$ to $B_y < 0$ by the inbox α effect. The radial field B_x is not concerned; $\boldsymbol{B} = (0, 0.1, 10)$, $\Omega = 10$, Pr = 0.1, Pm = 0.1, and $\theta = 45°$.

To sum up, by the α effect, the latitudinal angular momentum transport is formally increased for the positive inclination angle of the magnetic field (in the northern hemisphere). The 'real' stress values without this impact are thus smaller than the simulated values. The T_{yz} given in Table 1 (and also in Table 3) are thus maximal values. The corrections, however, are only small as for $p_y \ll 1$ and $p_y \gg 1$; the rotation-induced terms are basically larger than the Maxwell stress $B_y B_z$ for $\Omega = 0$. They are in particular small for models with $|p_y| \gg 1$.

Table 1. Latitudinal angular momentum transport $\tilde{T}_{yz}$ for very large or very small inclination angles, $p_y > 0$ in the upper two lines and $p_y < 0$ in the lower two lines. The last column gives the contribution for $\Omega = 0$, i.e., without both the α and Λ effect; $\Omega = 10$, Pr = Pm = 0.1, and $\theta = 45°$.

B_z	B_y	p_y	$\tilde{T}_{yz}$	$\tilde{T}_{yz}\|_{\Omega=0}$
20	0.1	$5 \cdot 10^{-3}$	0.0159	- 0.0030
0.1	20	200	0.0285	
-20	0.1	$-5 \cdot 10^{-3}$	0.0255	0.0030
-0.1	20	-200	0.0334	

In Table 1 data are given leading to the latitudinal flux T_{yz} of angular momentum. Different values of T_{yz} numerically result for the fields $\boldsymbol{B} = (0, 0.1, 20)$ and $\boldsymbol{B} = (0, 20, 0.1)$ if the box rotates with $\Omega = 10$. In all cases, $|B_y B_z| = 2$. The magnetic fields of all examples have the same total value of about 20. For the models in the upper two lines, the pitch angle p_y is positive. Also for negative p_y, that is for the fields $\boldsymbol{B} = (0, 0.1, -20)$ and $\boldsymbol{B} = (0, 20, -0.1)$ in the lower two lines, the results differ. The fluxes are only equal for zero rotation (the last column of the table). The differences are thus due to the α effect. They also differ for positive and for negative p_y, as it should; the flux is increased for negative $B_y B_z$.

It should be mentioned that the magnetic amplitude $B_z = 20$ represents a field almost in equipartition with the calculated turbulence rms velocity $u_{\mathrm{rms}} \simeq 5.3$. We also conclude from the numbers in Table 1 that for saturated magnetic fields the angular momentum transport by the Lorentz force is by far overcompensated for by the angular momentum transport of the rotating turbulence. The total stress is positive for all the given magnetic field examples, but it is smallest for the field with the positive solar value $p_y = 5 \cdot 10^{-3}$. The Lorentz force numbers for $\Omega = 0$ given in the last column of Table 1 only contribute to about 10% of the total stresses. For positive p_y, the T values with and without rotation even possess opposite signs. It becomes obvious here that the Malkus-Proctor effect does not play a major role in the angular momentum transport in stellar convection zones.

5. Rotating magnetoconvection

In a stratified medium, the (solid-body) rotation alone provides finite cross components of the Reynolds stress without any magnetic fields. The magnetic field, however, modifies these correlations and also enhances or reduces the angular momentum transport by the generation of Maxwell stresses.

Without magnetic fields, a rotation with $\Omega = 10$ produces cross-correlations of the normalised values $\tilde{Q}_{xz} = -0.062$ and $\tilde{Q}_{yz} = 0.024$ (from Table 3, first line) at a latitude of $\theta = 45°$. With numbers taken from Fig. 1 in both cases, the correlation coefficient $c = |Q_{ij}|/\sqrt{u_i^2 u_j^2}$ is about 0.5 for the given cross-correlations (see Fig.1). For fast rotation, the hydrodynamic ra-

dial Λ effect is negative (the angular momentum flows inwards), while the latitudinal Λ effect is always positive (the angular momentum flows equatorward). Basically, it is $|Q_{xz}| \gtrsim Q_{yz}$. The numerical values strongly depend on the latitude. By definition, both correlations vanish at the poles and T_{yz} also vanishes at the equator (Fig. 7). Under the influence of magnetic fields, the values are reduced ('magnetic quenching') depending on the inclination of the background fields. We shall assume in Eqs. (35) and (36) that the typical profiles in Fig. 7 are not changed by the magnetic influences.

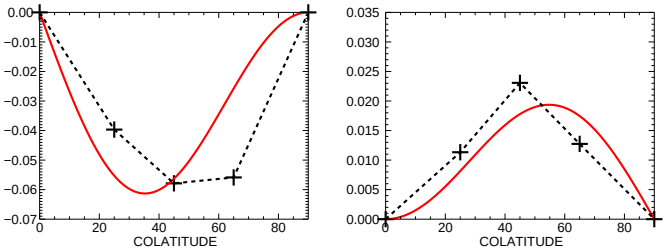

Fig. 7. Simulation results for the vertical angular momentum transport T_{xz} (left) and the latitudinal angular momentum transport T_{yz} (right) without magnetic fields ($\boldsymbol{B} = 0$) vs. colatitude θ. The red lines give the θ functions used in Eqs. (35) and (36). The crosses at $\theta = 45°$ reflect the values of Table 3 (first line); $\Omega = 10$, Pr = 0.1, and Pm = 0.1.

In order to formulate the magnetic influences on the angular momentum fluxes, we shall restrict our computations to midlatitudes ($\theta = 45°$). The influences on the latitudinal angular momentum transport T_{yz} are represented by Fig. 8, providing the total stresses as well as the Reynolds and both Maxwell stresses for the two inclined fields $\boldsymbol{B} = (0, \pm 1, 10)$. In both cases, the small-scale Maxwell stresses are only weak and the large-scale Maxwell stresses are of opposite sign. The main result is that for both magnetic configurations, the T_{yz} are positive in opposition to nonrotating turbulence (see Fig. 4), hence with rotation the Reynolds stresses dominate the Lorentz force.

For $B_y B_z > 0$, the Reynolds stress grows and for $B_y B_z < 0$ it sinks, that is the coefficient D in Eq. (13) is positive in opposition to D^* in Eq. (14) which becomes negative. The small numerical value indicates a reduced effectivity of the mean field Lorentz force to transport angular momentum. It is thus very questionable that a theoretical explanation of the solar torsional oscillation with only the action of the dynamo-induced Lorentz force may work.

The code was also probed with the radial flux T_{xz} for an inclined magnetic field $B_z = 10$ with components B_x varying between ±1 and ±10 (Table 2). Here the nonmagnetic value of $\tilde{T}^*_{xz} = -0.062$ was magnetically reduced to $\tilde{T}^*_{xz} = -0.029$ by the field $\boldsymbol{B} = (\pm 10, 0, 10)$. This is a clear but mild magnetic quenching. For $B_x = 1$ and $B_z = 10$, the equipartion value of the field is $\beta = 0.50$ and for $B_x = B_z = 10$ it is $\beta = 0.75$ with β^2 as the ratio of magnetic to kinetic energy. The reported quenching behaviour is similar to that of Käpylä (2019) in a quite different approach. We also find that the coefficient $\tilde{D}^*$ is basically uninfluenced by the magnetic background field. For very strong fields the mean value $\tilde{T}^*_{xz}$ vanishes, while $\tilde{D}^* \to -0.018$ known from Section 3 for $\Omega = 0$. The main result is thus that for small fields $|B_x|$, the flux T_{xz} is always negative but for large $|B_x|$, when the Lorentz force dominates, both signs appear indicating that the Reynolds stress is smaller than the Maxwell stress.

Table 2. Results for the vertical flux $\tilde{T}_{xz}$ (averaged over radius and time) with $B_z = 10$, $\Omega = 10$, Pr = Pm = 0.1, and $\theta = 45°$.

B_z	B_x	$\tilde{T}_{xz}$	$\tilde{T}^*_{xz}$	$\tilde{D}^*$	$T_{xz}/Q_{xz}\|_{B=0}$	$\tilde{T}_{xz}\|_{\Omega=0}$
0	0		-0.062			
10	1	-0.059			0.95	0.0023
			-0.049	-0.013		
10	-1	-0.038			0.61	-0.0023
10	10	-0.15			2.4	0.023
			-0.029	-0.014		
10	-10	0.09			-1.4	-0.023

All correlations are written in units of the reference turbulence intensity $u^2_{\rm rms} = 28$ resulting from the nonrotating and unmagnetised turbulent fluid. With $\Omega = 10$, we used a rather fast rotation rate in order to minimise the large-scale shear flows which develop in the turbulent box (Brummell et al. 1998). The faster the rotation is, the weaker the shear of these flows and the smaller their influence onto the calculated correlations. As demonstrated by Rüdiger et al. (2019), both the calculated nondiffusive fluxes V and H are minimum values; they would be slightly larger under suppression of the action of the induced shear flows.

We note that the modified Lorentz force factor D^* is always negative and (almost) independent of the magnetic inclination angle. It only grows for very small angles, and it depends on B_x only for $|B_x| \ll |B_z|$ when its amount becomes smaller. The dependence on B_x vanishes for larger values. The consequence is that for $|B_x| \ll |B_z|$ the magnetic quenching of Q_{xz} cannot be compensated for by the Lorentz force $B_x B_z$ so that the total sum T_{xz} becomes smaller than the unmagnetised value $Q_{xz}(B = 0)$ as shown in the next to last column of Table 2. This behaviour is the natural counterpart to the phenomenon of negative effective-magnetic-pressure where total pressure is also reduced by the magnetic parts, but only for a weak magnetic field (Brandenburg et al. 2011; Käpylä et al. 2012; Rüdiger et al. 2012). Here, the magnetic-induced reduction of the total angular momentum transport happens for $B_x \lesssim 0.1 B_z$ (similar for B_y).

The main results of the simulations for $B_z = 20$ and various B_x and B_y are summarised in Table 3. The reference values of the nonmagnetic approximation are given in the first row of the table. The last columns in the table (also in boldface) give the fluxes due to the Lorentz force alone without rotation. The underlined numbers provide the resulting angular momentum fluxes with rotation and the equipartition field $B_z = 20$ and $B_x = \pm 0.1$ or $B_y = \pm 0.1$. For the given rotation rate and the magnetic field geometry, the resulting angular momentum transport is dominated by the turbulence rather than by the Lorentz force of the background field. The magnetic influence on the total stresses is, nevertheless, remarkably strong. The interplay of rotation, magnetic fields, and turbulence mainly leads to a suppression of the turbulence-induced angular momentum transport despite the contribution of the large-scale Lorentz force. The underlined numbers in Table 3 demonstrate how the turbulent transport is suppressed by the inclined field with the given components. The vertical transport T_{xz} for both signs of B_x lies below the hydrodynamic value. The horizontal transport T_{yz} is also suppressed, but there is a difference for positive and negative B_y.

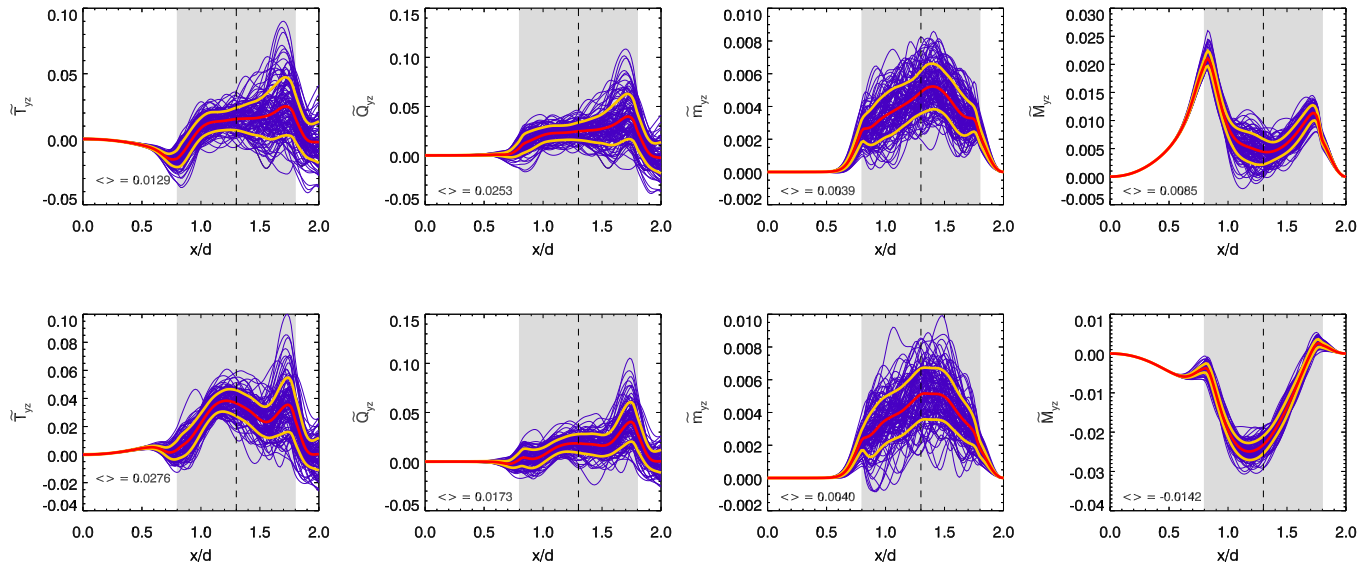

Fig. 8. Snapshots of the (yz)-correlations (normalised with $u_{\rm rms}^2 = 28$) for $\Omega = 10$ and a magnetic field $\boldsymbol{B} = (0, 1, 10)$ (top) or $\boldsymbol{B} = (0, 1, -10)$ (bottom). From left to right: $\tilde{T}_{yz}$, $\tilde{Q}_{yz}$, $\tilde{m}_{yz}$, and M_{yz}. In opposition to nonrotating turbulence (see Fig. 4), T_{yz} is now positive for both field geometries. As Käpylä et al. (2017) show with their numerical dynamo simulations, the numerical values of the two middle rows are rather robust against the variation of the magnetic Prandtl number; Pr = 0.1, Pm = 0.1, and $\theta = 45°$.

In the latter case, the magnetic and the nonmagnetic T_{yz} hardly differ, while for positive B_y the suppression is very strong. The signs of the total fluxes never differ for different signs of the (small) inclination angles p.

6. Rotation laws

To obtain the (axisymmetric) rotation law $\Omega = \Omega(r, \theta)$ in the solar convection zone, the equation for the conservation of angular momentum in spherical coordinates

$$\rho r^2 \sin^2\theta \frac{\partial \Omega}{\partial t} + \mathrm{div}\ \boldsymbol{t} = 0 \tag{31}$$

was solved using a time-dependent finite difference code and the density profile of the solar convection zone with variations of three orders of magnitudes. The relevant components of the angular momentum flux vector $\boldsymbol{t}$ are

$$t_r = r \sin\theta \rho \left(Q^\nu_{r\phi} + T_{r\phi} \right), \tag{32}$$

$$t_\theta = r \sin\theta \rho \left(Q^\nu_{\theta\phi} + T_{\theta\phi} \right) \tag{33}$$

with the viscous part of the stress tensor

$$Q^\nu_{r\phi} = -\nu_{\rm T} r \sin\theta \frac{\partial \Omega}{\partial r}, \qquad Q^\nu_{\theta\phi} = -\nu_{\rm T} \sin\theta \frac{\partial \Omega}{\partial \theta} \tag{34}$$

and constant viscosity coefficient $\nu_{\rm T}$. The boundary conditions at the top and bottom of the convection zone are simply $t_r = 0$. They ensure that no angular momentum leaves the convection zone. We note that the angular momentum transport by the meridional flow was neglected here so that only the azimuthal component (31) of the Reynolds equation must have been solved. The complete mean-field theory on the basis of Eq. (33) provides one-cell meridional flows circulating counterclockwise in the northern hemisphere (Rüdiger et al. 2013) close to the recent results of helioseismology (Gizon et al. 2020).

The code started with rigid rotation and was run until a stationary solution was reached. The latitudinal profiles in Fig. 7 are the basis for the formulation

$$\tilde{T}_{xz} = V \cos^2\theta \sin\theta \tag{35}$$

with the minimum at $\theta = 35°$ and

$$\tilde{T}_{yz} = H \cos\theta \sin^2\theta, \tag{36}$$

with the maximum at $\theta = 54°$. The V and H are dimensionless quantities. They are coupled to the viscosity term in the angular momentum equation by a dimensionless factor $\zeta = u_{\rm rms}^2/\nu_{\rm T}\Omega$ for which solar values provide $\zeta \lesssim 10$. The parameter ζ includes all normalisation factors, hence $T_{r\phi} := \zeta \tilde{T}_{xz}$ and $T_{\theta\phi} := \zeta \tilde{T}_{yz}$.

Equation (35) contains the nontrivial assumption that the radial turbulent transport vanishes at the equator, which is the case for quasilinear analytical calculations without magnetic fields (Rüdiger et al. 2013). We do not expect contradictions by the magnetic fields as the toroidal background field vanishes at the equator. However, without meridional circulation and without turbulence-induced anisotropic heat transport, the immediate consequence of vanishing radial flux along $\theta = 90°$ is the uniformity of Ω in the equatorial plane in contrast to the slight superrotation which is observed with methods of helioseismology. This little disadvantage of our model may be accepted by the reader.

The coefficients V and H in Eqs. (35) and (36) were calculated from the numerical results in Table 3 for $\theta = 45°$. For a rotating but nonmagnetic box, one finds from the first line of Table 3 the values $V = -0.18$ and $H = 0.066$. The radial flux exceeds the latitudinal one by a factor of three. The resulting isolines of the angular velocity $\Omega(r, \theta)$ are given by a red colour in the plots of Fig. 9. In the spirit of the Malkus-Proctor approximation, the nonmagnetic rotation law may be modified only by the large-scale Lorentz force of the two fields $\boldsymbol{B} = (0, \pm 0.1, 20)$ (blue lines). We note again that $B_z = 20$ represents the equipartition value of the azimuthal field, while $B_y = \pm 0.1$ is still a rather large value for the possible latitudinal field component. The formally resulting momentum fluxes are $H = 0.058$ for $B_y = 0.1$

Table 3. Normalised angular momentum fluxes $\tilde{T}_{xz}$ and $\tilde{T}_{yz}$ (averaged over radius and time) with $B_z = 20$ and for various meridional magnetic field components B_x and B_y. The boldfaced numbers give the correlations without a field (first line) and without rotation (last columns); $\Omega = 10$, Pr = Pm = 0.1, and $\theta = 45°$.

B_z	B_x	p_x	$\tilde{T}_{xz}$	$\tilde{T}^*_{xz}$	$\tilde{T}_{xz}\|_{\Omega=0}$	B_y	p_y	$\tilde{T}_{yz}$	$\tilde{T}^*_{yz}$	$\tilde{T}_{yz}\|_{\Omega=0}$
0	0	-	-0.0623	-	0	0	-	0.0235	-	0
20	0.05	0.0025	-0.0541	-0.051	0.00023	0.05	0.0025	0.0201	0.023	-0.0015
20	-0.05	-0.0025	-0.0475		-0.00023	-0.05	-0.0025	0.0262		0.0015
20	0.1	0.005	-0.0537	-0.053	0.00046	0.1	0.005	0.0159	0.021	-0.0030
20	-0.1	-0.005	-0.0498		-0.00046	-0.1	-0.005	0.0255		0.0030
20	1	0.05	-0.073	-0.049	0.0046	1	0.05	0.00829	0.025	-0.030
20	-1	-0.05	-0.026		-0.0046	-1	-0.05	0.0424		0.030

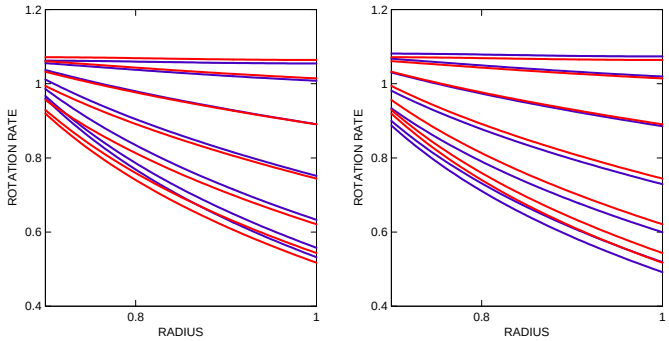

Fig. 9. Rotation laws in radius r and colatitude θ for fast rotation ($\Omega = 10$) under the influence of the large-scale Lorentz force for $\boldsymbol{B} = (0, 0.1, 20)$ (left panel, blue lines) and $\boldsymbol{B} = (0, -0.1, 20)$ (right panel, blue lines). The differential rotation is due to the nonmagnetic Λ effect (red lines). The uppermost Ω-isolines belong to the equator, while the lowest curves belong to the poles.

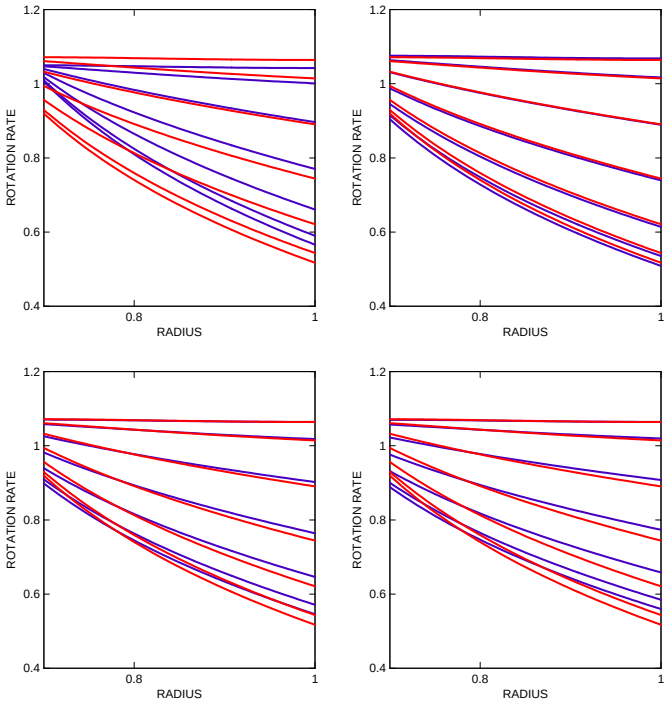

Fig. 10. Similar to Fig. 9, but with the total magnetic stress-tensor from Eq. (8). The applied magnetic fields (at $\theta = 45°$) are $\boldsymbol{B} = (0, 0.1, 20)$ (top left, model 1), $\boldsymbol{B} = (0, -0.1, 20)$ (top right, model 2), $\boldsymbol{B} = (0.1, 0, 20)$ (bottom left, model 3), and $\boldsymbol{B} = (-0.1, 0, 20)$ (bottom right, model 4). The red curves are the nonmagnetic rotation laws.

and $H = 0.075$ for $B_y = -0.1$. Fields with a positive inclination angle transport the angular momentum poleward and fields with a negative inclination angle transport the angular momentum equatorward. In general, the field with the positive inclination angle (as in the solar convection zone) reduces the latitudinal shear, while the field with the negative inclination angle enhances the shear. There is even a tendency of a magnetic deceleration of the equatorial rotation rate but this is only a very small effect which becomes even weaker as B_y diminishes. To include the magnetic background fields in a consistent way, the underlined coefficients in Table 3 must be used to evaluate the coefficients V and H for $p_x = p_y = \pm 5 \cdot 10^{-3}$. In Fig. 10 the blue lines again represent the rotation laws under the influence of these magnetic fields, while the red lines are valid for $\boldsymbol{B} = 0$.

In Table 4, the four models with different magnetic geometries are summarised for which the rotation laws have been calculated. All models work with the equipartition value $B_z = 20$ and with the inclination angles $|p| = 5 \cdot 10^{-3}$. We focus our attention to the model 1 with positive $B_y B_z$, which should be most reliable for the solar convection zone. The combinations of B_x and B_z are much more speculative.

The rotation laws for models 1–4 are displayed in Fig. 10. The lines represent the rotation rates within the convection zone for various latitudes. The uppermost profiles belong to the equator, while the lowest lines belong to the poles. All models provide the magnetic-suppression of the equator-pole difference of the surface rotation. The spread of the (non-magnetic) red lines exceeds that of the (magnetic) blue lines for all models except for model 2 where the magnetic influence is basically weak. Only in one case, however, is the equatorial rotation rate also magnetically reduced. This is true for model 1 where the upper blue

Table 4. Vertical and the horizontal fluxes of angular momentum for various combinations of the meridional magnetic field components; Ω = 10 and Pr = Pm = 0.1.

model	B_x	B_y	B_z	V	H
0	0	0	0	-0.18	0.066
1	0	0.1	20	-0.18	0.045
2	0	-0.1	20	-0.18	0.072
3	0.1	0	20	-0.15	0.066
4	- 0.1	0	20	-.0.14	0.066

line clearly lies below the upper red line, hence the equator rotates slower during the magnetic activity maximum. For all other magnetic configurations, the equatorial rotation rate is magnetically uninfluenced. Obviously, the deceleration of the equator is a consequence of the magnetic quenching which reduces the horizontal transport coefficient down to $H = 0.045$. Model 1 shows the magnetic-originated variation of the equator-pole difference of Ω as 3–4 units of the magnetic-originated variation of the equatorial rotation rate so that not only the first observational condition as shown in Eq. (3) but also the second one will approximately be fulfilled by model 1.

7. Results and discussion

The explanation of a possible non-regular behaviour in the magnetic activity cycle has been started including the magnetic feedback on the internal solar rotation. Jennings & Weiss (1991), Kitchatinov et al. (1994), and Tobias (1996) added the conservation law of angular momentum in the turbulent convection zone to the dynamo equations including magnetic feedback in order to simulate the interplay of induced magnetic fields and rotation. The form of the rotation law can be influenced by the magnetic field in two ways. If the magnetic field only consists on a (strong) toroidal field, then the Reynolds stress (Λ effect and/or eddy viscosity) is magnetically quenched. If, however, the magnetic field also possess (weak) latitudinal components then small-scale as well as large-scale Maxwell stresses additionally contribute to the angular momentum transport. Yoshimura (1981), Schüssler (1981), Noyes et al. (1984), and Rüdiger et al. (1986) presented the first dynamo models where large-scale Lorentz forces due to induced magnetic fields modified the internal rotation laws.

In the present paper, the total angular momentum transport by rotating magnetoconvection under the influence of prescribed magnetic background fields was calculated by means of 3D MHD box simulations. They are motivated by the observational result that in the solar activity maximum both the equator-pole difference of the surface rotation rate and the equatorial rotation rate is reduced where the latter has only a 1% effect. The question is whether a combination of a (strong) azimuthal field component as well as (weak) radial and latitudinal field components can reproduce these observations.

A natural start of the calculations is given by Fig. 9. The magnetic modifications of the rotation profiles are only due to the large-scale Lorentz force of two prescribed large-scale fields, which is the original configuration used by Malkus & Proctor (1975). The (dominating) azimuthal field with energy in equipartition with the kinetic energy of the turbulence is $B_z = 20$. If the extra latitudinal field $B_y = 0.1$ is added, the resulting Maxwell stress transports the angular momentum poleward and the latitudinal shear is magnetically reduced. It is clear that for $B_y = -0.1$, the opposite is true: The shear is increased. These results are almost trivial and for decreasing $|B_y|$ they disappear.

The calculations have been repeated with the total stresses shown in Eqs. (9) and (10), which are known from box simulations for rotating convection under the influence of magnetic background fields of the same geometry. Then Reynolds stress, small-scale Maxwell stress, and large-scale Maxwell stress are the transporters of the angular momentum. The numerical simulations lead to the two main results that i) the influence of the large-scale Maxwell stress is only small, that is $T_{yz} \gg T_{yz}|_{\Omega=0}$, and ii) the magnetic influence on the Reynolds stress depends on the sign of B_y, that is $T_{yz} < T_{yz}|_{B=0}$ for $B_y = 0.1$ and $T_{yz} \gtrsim T_{yz}|_{B=0}$ for $B_y = -0.1$. Consequently, the equator-pole difference of Ω is almost not influenced if $B_y B_z < 0$, but it is strongly reduced if $B_y B_z > 0$ (see top panel of Fig. 10). In the latter case, the equator is also decelerated in the activity maximum. Positive $B_y B_z$ is expected to exist within the solar convection zone and the resulting magnetic behaviour of the rotation law with an accelerated equator fully complies with the observations shown in Eq. (3). The scenario appears to be consistent in the following case: If magnetic fields B_θ exist, the turbulence-originated rotational shear produces positive products of $B_\theta B_\phi$ which, in agreement with the observations, simultaneously reduce the equatorial value of the angular velocity and the surface differential rotation. It is also obvious that for the Sun the angular momentum transport by the Maxwell stress does not exceed the transport by the Reynolds stress. With $u_r \simeq u_\phi \simeq 100$ m/s and with $B_r \simeq 1$ Gauss and $B_\phi \simeq 10^4$ Gauss, one finds the ratio $B_r B_\phi/(\mu_0 \rho c u_r u_\phi) \lesssim O(10^{-2})$ where the correlation factor $c \simeq 0.1$ and the density $\rho \simeq 10^{-2}$ gcm^{-3} have approximately been used. Indeed, the solar observations reveal the cycle-dependent velocity variations as never exceeding the 10^{-2} limit. One would need toroidal fields of the order of 10^{5-6} Gauss in order to find the rotation law as basically modulated by the Lorentz force.

As our model of the solar differential rotation is stationary and the latitude dependence of the Reynolds stress is completely determined through the V and H coefficients, it cannot be directly used for the explanation of the torsional oscillation patterns. Howard & Labonte (1980) determined a global rotation law, which they subtracted from the observed profile of the rotation rate. The residual shows a pattern of alternating bands of fast and slow rotation. Zones of more rapid rotation appear at high latitude and migrate towards the equator similar to the active regions. More recent observations revealed that the zone of faster than average rotation reaches the equator in the solar minimum (Basu & Antia 2003; Howe et al. 2011). This is in line with the findings in the present paper.

References

Augustson, K., Brun, A. S., Miesch, M., & Toomre, J. 2015, The Astrophysical Journal, 809, 149

Basu, S. & Antia, H. M. 2003, The Astrophysical Journal, 585, 553

Brandenburg, A., Kemel, K., Kleeorin, N., Mitra, D., & Rogachevskii, I. 2011, ApJ, 740, L50

Browning, M. K., Miesch, M. S., Brun, A. S., & Toomre, J. 2006, ApJ, 648, L157

Brummell, N. H., Hurlburt, N. E., & Toomre, J. 1998, The Astrophysical Journal, 493, 955

Brun, A. S., Miesch, M. S., & Toomre, J. 2004, The Astrophysical Journal, 614, 1073

Chandrasekhar, S. 1961, Hydrodynamic and hydromagnetic stability (Oxford: Clarendon)

Featherstone, N. A. & Miesch, M. S. 2015, The Astrophysical Journal, 804, 67
Gilman, P. A. & Howard, R. 1984, The Astrophysical Journal, 283, 385
Gizon, L., Cameron, R. H., Pourabdian, M., et al. 2020, Science, 368, 1469
Howard, R. & Labonte, B. J. 1980, ApJ, 239, L33
Howe, R., Hill, F., Komm, R., et al. 2011, in Journal of Physics Conference Series, Vol. 271, GONG-SoHO 24: A New Era of Seismology of the Sun and Solar-Like Stars, 012074
Jennings, R. L. & Weiss, N. O. 1991, Month. Not. Roy. Astr. Soc., 252, 249
Jurdana-Šepić, R., Brajša, R., Wöhl, H., et al. 2011, Astronomy & Astrophysics, 534, A17
Käpylä, M. J., Käpylä, P. J., Olspert, N., et al. 2016, Astronomy & Astrophysics, 589, A56
Käpylä, P. J. 2019, Astronomy & Astrophysics, 622, A195
Käpylä, P. J., Brandenburg, A., Kleeorin, N., Mantere, M. J., & Rogachevskii, I. 2012, Month. Not. Roy. Astr. Soc., 422, 2465
Käpylä, P. J., Käpylä, M. J., Olspert, N., Warnecke, J., & Brandenburg, A. 2017, Astronomy & Astrophysics, 599, A4
Käpylä, P. J., Korpi, M. J., & Brandenburg, A. 2009, Astronomy & Astrophysics, 500, 633
Käpylä, P. J., Korpi, M. J., & Tuominen, I. 2004, Astronomy & Astrophysics, 422, 793
Karak, B. B., Käpylä, P. J., Käpylä, M. J., et al. 2015, Astronomy & Astrophysics, 576, A26
Kippenhahn, R. 1963, The Astrophysical Journal, 137, 664
Kitchatinov, L. L. & Rüdiger, G. 1995, Astronomy & Astrophysics, 299, 446
Kitchatinov, L. L., Rüdiger, G., & Küker, M. 1994, Astronomy & Astrophysics, 292, 125
Küker, M. & Rüdiger, G. 2018, Astronomische Nachrichten, 339, 447
Malkus, W. V. R. & Proctor, M. R. E. 1975, Journal of Fluid Mechanics, 67, 417
Miesch, M. S., Brun, A. S., & Toomre, J. 2006, The Astrophysical Journal, 641, 618
Noyes, R. W., Weiss, N. O., & Vaughan, A. H. 1984, The Astrophysical Journal, 287, 769
Ossendrijver, M., Stix, M., & Brandenburg, A. 2001, Astronomy & Astrophysics, 376, 713
Ossendrijver, M., Stix, M., Brandenburg, A., & Rüdiger, G. 2002, Astronomy & Astrophysics, 394, 735
Rüdiger, G. 1974, Astronomische Nachrichten, 295, 275
Rüdiger, G., Kitchatinov, L. L., & Hollerbach, R. 2013, Magnetic Processes in Astrophysics: theory,simulations, experiments (Wiley-VCH)
Rüdiger, G., Kitchatinov, L. L., & Schultz, M. 2012, Astronomische Nachrichten, 333, 84
Rüdiger, G., Küker, M., Käpylä, P. J., & Strassmeier, K. G. 2019, Astronomy & Astrophysics, 630, A109
Rüdiger, G., Tuominen, I., Krause, F., & Virtanen, H. 1986, Astronomy & Astrophysics, 166, 306
Ruždjak, D., Brajša, R., Sudar, D., Skokić, I., & Poljančić Beljan, I. 2017, Sol. Phys., 292, 179
Schüssler, M. 1981, Astronomy & Astrophysics, 94, L17
Tobias, S. M. 1996, Astronomy & Astrophysics, 307, L21
Warnecke, J. 2018, Astronomy & Astrophysics, 616, A72
Warnecke, J., Rheinhardt, M., Tuomisto, S., et al. 2018, Astronomy & Astrophysics, 609, A51
Xie, J., Shi, X., & Qu, Z. 2018, The Astrophysical Journal, 855, 84
Yoshimura, H. 1981, The Astrophysical Journal, 247, 1102
Ziegler, U. 2004, Journal of Computational Physics, 196, 393